



Analysis of BMR Tilt from AutoTAB Catalog: Hinting toward the Thin Flux Tube Model?

Anu Sreedevi¹ , Bibhuti Kumar Jha^{2,3} , Bidya Binay Karak¹ , and Dipankar Banerjee^{3,4,5}

¹ Department of Physics, Indian Institute of Technology (Banaras Hindu University), Varanasi 221005, India; anubsreedevi.rs.phy20@itbhu.ac.in, karak.phy@iitbhu.ac.in

² Southwest Research Institute, Boulder, CO 80302, USA

³ Aryabhata Research Institute of Observational Sciences, Nainital 263002, Uttarakhand, India

⁴ Indian Institute of Astrophysics, Koramangala, Bangalore 560034, India

⁵ Center of Excellence in Space Sciences India, IISER Kolkata, Mohanpur 741246, West Bengal, India
Received 2024 February 5; revised 2024 March 14; accepted 2024 March 15; published 2024 April 29

Abstract

One of the intriguing mechanisms of the Sun is the formation of bipolar magnetic regions (BMRs) in the solar convection zone (CZ), which are observed as regions of concentrated magnetic fields of opposite polarity on the photosphere. These BMRs are tilted with respect to the equatorial line, which statistically increases with latitude. The thin flux tube model, employing the rise of magnetically buoyant flux loops and their twist by Coriolis force, is a popular paradigm for explaining the formation of tilted BMRs. In this study, we assess the validity of the thin flux tube model by analyzing the tracked BMR data obtained through the Automatic Tracking Algorithm for BMRs. Our observations reveal that the tracked BMRs exhibit the expected collective behaviors. We find that the polarity separation of BMRs increases over their normalized lifetime, supporting the assumption of a rising flux tube from the CZ. Moreover, we observe an increasing trend of the tilt with the flux of the BMR, suggesting that rising flux tubes associated with lower flux regions are primarily influenced by drag force and Coriolis force, while in higher flux regions, magnetic buoyancy dominates. Furthermore, we observe Joy's law dependence for emerging BMRs from their first detection, indicating that at least a portion of the tilt observed in BMRs can be attributed to the Coriolis force. Notably, lower flux regions exhibit a higher amount of fluctuations associated with their tilt measurement compared to stronger flux regions, suggesting that lower flux regions are more susceptible to turbulent convection.

Unified Astronomy Thesaurus concepts: [Bipolar sunspot groups \(156\)](#); [Solar activity \(1475\)](#); [Solar physics \(1476\)](#); [Solar magnetic fields \(1503\)](#); [Solar active region magnetic fields \(1975\)](#)

1. Introduction

The bipolar magnetic regions (BMRs), commonly observed in line-of-sight (LOS) magnetograms, emerge on the solar surface in an east–west orientation with a finite tilt having the leading polarity closer to the equator (Hale et al. 1919). Statistically, BMR tilt increases with the latitude of emergence, which is commonly referred to as Joy's law. This behavior was validated by many authors, including Howard (1991), Wang & Sheeley (1991), and Sivaraman et al. (1999), using white-light observations prior to the availability of magnetograms. The tilt in the BMRs plays an essential role in the reversal of the existing poloidal field through the dispersal and cancellation of fluxes on the solar surface (Babcock 1961; Leighton 1964). This process is popularly known as the Babcock–Leighton mechanism and is an essential component of the solar dynamo (e.g., Cameron & Schüssler 2023; Karak 2023).

Our present understanding attributes the formation of BMRs to the magnetically buoyant, large-scale toroidal flux tubes generated by the solar dynamo process at the base of the convection zone (BCZ; Parker 1955). Numerical simulation studies, assuming the thin flux tube approximation, have focused on understanding the dynamics of Ω -shaped flux tubes and provide constraints to the magnetic field strength in the

convection zone (CZ; Caligari et al. 1995; Fan 2009). The works of D'Silva & Choudhuri (1993) and Fan et al. (1994) demonstrate that the tilt in the BMR is due to the action of Coriolis force on the diverging flows at the apex of rising flux tubes. Consequently, stronger BMRs, with higher magnetic field strength at the BCZ, are expected to ascend rapidly through the CZ and experience Coriolis force for less time, leading to a reduced amount of tilt in them. Their works also predicted that with the increase of the flux in the tube, the BMR tilt increases, due to the effect of the drag. Observational studies, such as that by Tian et al. (2003), using magnetic field observations from the Huairou Solar Observatory Station, validate these findings, noting an initial increase in tilt angle with flux followed by a decrease for higher flux BMRs. Similar variations in tilt angle with magnetic field strength are observed in simulations by Weber et al. (2011) and in observational studies by Jha et al. (2020). Interestingly, Stenflo & Kosovichev (2012) did not find any systematic dependence of tilt on flux from LOS magnetic field observations of the Michelson Doppler Imager (MDI).

The theory of the Coriolis force as the reason behind tilted BMR is very promising and has been studied extensively. If this theory is true, then BMRs should emerge on the photosphere with a definite tilt. Analyzing 715 BMRs from MDI magnetograms during 1996–2008, Kosovichev & Stenflo (2008) found Joy's law behavior of BMR tilts at their mid-emergence phase, concluding, “The observations indeed show the predicted latitudinal dependence (Joy's law) and indicate

that the tilt is formed below the surface.” Later, Schunker et al. (2020) noted that BMRs emerge with zero tilt and develop tilt in accordance with Joy’s law at a later stage in their lifespan, challenging the thin flux tube model’s prediction. They suggested that the observed Joy’s law behavior is because of the inherent north–south separation of BMRs as they reach the surface.

Joy’s law is statistical, and thus, the latitudinal dependency of tilt is evident after averaging over large data samples. Persistent, significant scatter around Joy’s law has consistently been observed in various observational studies across different data sets (e.g., Wang & Sheeley 1991; Howard 1996; Dasi-Espuig et al. 2010; McClintock & Norton 2013). Fan et al. (1994) and Longcope & Fisher (1996) hint toward the role of turbulent convection on rising flux tubes as the possible cause of the scatter in tilt angle. This observed behavior was further supported by the simulation of Weber et al. (2013). Recently, a thorough analysis of the inconsistencies in Joy’s law has been explored by Will et al. (2023).

Currently, observational support for the thin flux tube model is very limited and not adequate enough to establish their existence. The lack of dependence of BMR’s tilt on flux has been used to strongly rule out the thin flux tube model based on the studies presented in Kosovichev & Stenflo (2008) and Schunker et al. (2019). While the latter study was based on a limited data set, the study of Stenflo & Kosovichev (2012) did not include the tracked information of BMRs, and hence, they counted every detection of BMR as a new one, giving a higher weightage to long-living BMRs (bigger ones). On the basis of all these results, we are still not in a position to completely rule out the thin flux tube model.

This manuscript aims to understand the origin mechanism of BMRs using the tracked BMR information from the Automated Tracking Algorithm for BMRs (AutoTAB; Jha et al. 2021; Sreedevi et al. 2023) catalog, which contains the tracked information of 12,173 unique BMRs during the period of 1996–2023. We study the general behavior of BMR properties over their lifetime and explore the validity of the thin flux tube model. Before we present our study, in Section 2, we list what kind of observational signatures we expect based on this theory. Then, in Section 4, we present our results, followed by conclusions in Section 5.

2. Observational Expectations for the Thin Flux Tube Model

The simplest explanation for the formation of the BMR is given by the thin flux tube model (Parker 1955). The model assumes a thin, untwisted flux tube with a diameter that is negligible compared to the length scale of the perturbation in the tube, anchored in the deep CZ. Upon becoming magnetically buoyant, tubes rise through the CZ to the photosphere. If the flux tubes remain anchored in the CZ, they rise in the form of an Ω -shaped loop structure. As the flux tubes rise, the draining plasma from the apex of the tube is subjected to the Coriolis force, which leads to the observed tilt in the BMRs (D’Silva & Choudhuri 1993).

Therefore, if Ω -shaped loops do exist and they are responsible for the formation of the BMRs, one can verify this idea by tracking the separation of BMR’s opposite polarities during the initial phases of their evolutions. We expect the polarities to separate as BMRs mature, indicating the rise of the Ω loop when observed in LOS magnetograms.

Second, if the Coriolis force acts on the rising flux tubes, then the leading polarity of the BMR is expected to be closer to the equator, and BMR’s tilt will have a latitudinal dependency (e.g., see Section 2 of D’Silva & Choudhuri 1993 for rough calculations). In such a scenario, we anticipate the BMRs will emerge with a definite tilt, and they are expected to follow Joy’s law, due to the pronounced effect of the Coriolis force in the CZ.

Finally, BMRs with higher flux are expected to have higher tilt, as predicted by the empirical relation given in Fan et al. (1994) for the tilt angle (γ),

$$\gamma \propto \sin \lambda B_0^{-5/4} \Phi^{1/4}. \quad (1)$$

Here, B_0 is the initial magnetic field in the flux tube (forming BMR) at the BCZ, Φ is the magnetic flux inside the rising flux tubes, and λ is the emerging latitude of the flux tube.

We note that, in the above model (Equation (1)), B_0 and the Φ are made independent of each other, while in the Sun, this may not be true. Nevertheless, based on the above relation, we expect that the tilt (γ) decreases with the increase of magnetic field strength (B_0). Although the magnetic flux that is measured in the BMR (Φ_m) is not exactly the same as Φ , they are expected to be related. However, for the magnetic field, it is not obvious; the field that is observed in the BMR on the solar surface is quite different from the initial field B_0 of the flux tube. Despite this, we shall also check the dependence of tilt with the measured magnetic field in addition to the dependency on the flux in the BMR. To the best of our knowledge, no definitive observational evidence supporting the thin flux tube model has been conclusively confirmed. In Section 4, using the AutoTAB catalog, we evaluate whether the BMR properties align with the mentioned findings from the thin flux tube model.

3. Data and Method

We start with a brief description of the AutoTAB catalog (Sreedevi & Jha 2023; Sreedevi et al. 2023) analyzed in this study. The catalog encompasses tracked information of 12,173 BMRs during 1996–2023, generated using AutoTAB. These tracked BMRs are observed in the LOS magnetograms from MDI (1996–2011; Scherrer et al. 1995, full cadence) and Helioseismic and Magnetic Imager (HMI; 2010–present; Scherrer et al. 2012, 96 minute cadence) on board the Solar and Heliospheric Observatory (SOHO) and Solar Dynamic Observatory (SDO), during the period of 1996 September–2023 December which includes complete Cycles 23 and 24, and early 25. The operation of AutoTAB is summarized below, while the details are published in Sreedevi et al. (2023).⁶

To automatically detect the BMRs from the LOS magnetogram, AutoTAB uses a method similar to that prescribed by Stenflo & Kosovichev (2012), which was also adopted by Jha et al. (2020) with slight modifications. All the detected regions satisfy the flux balance condition, similar to that in Stenflo & Kosovichev (2012) and Jha et al. (2020), to ensure that the amount of positive and negative flux are balanced in each BMR. This flux balance condition only checks for the amount of flux (positive and negative), rather than the distribution of flux in BMRs. Hence, the AutoTAB catalog (this work) also includes the multipolar regions, which are very frequent and

⁶ The AutoTAB catalog will be publicly available along with the codes at <https://github.com/sreedevi-anu/AutoTAB>.

thus important in contributing to the polar field in the Sun (Yeates 2020). The detected BMRs are saved as binary files, and AutoTAB uses these files to track the detected regions. These regions undergo preprocessing steps before the tracking for improved tracking efficiency, followed by the technique of feature association in successive binary files to track the BMR in future instances; see Sections 2.2 and 2.3 in Sreedevi et al. (2023) for details of AutoTAB. It has to be noted that the detection and tracking algorithms operate independently. Therefore, AutoTAB gives users the freedom to choose different methods of detection for BMRs or any other features, which can be efficiently tracked by AutoTAB.

AutoTAB tracks BMRs through their evolution on the nearside of the Sun, and the tracked BMRs have a wide range of lifetimes,⁷ which includes those tracked from emergence to decay, those tracked in their evolutionary stages only, and a small category of BMRs that live for less than 8 hr (mostly the ephemeral regions). These three groups have respectively been classified as lifetime (LT), disk passage (DP), and short lived (SL) by Sreedevi et al. (2023). The BMRs falling in the latter class are excluded from this study and will be explored in detail in a forthcoming manuscript. Lifetime BMRs are mostly composed of moderately small BMRs within the flux range of 10^{20} – 10^{22} Mx; some of them may not produce enough contrast in white-light images to be visible as sunspots. Meanwhile, the DP class constitutes BMRs, which have only been tracked during their appearance on the nearside of the Sun. Therefore, this class includes (i) BMRs that are first detected near the east limb ($<45^\circ$ E) and disperse on the nearside; (ii) BMRs that emerge on the nearside of the Sun but cross the west limb ($>45^\circ$ W); and (iii) BMRs that were first detected near the east limb ($<45^\circ$ E) and cross the west limb ($>45^\circ$ W). Hence, this class mainly comprises larger and stronger BMRs, exhibiting consistent evolution of magnetic properties throughout their lifetimes. The majority of the tracked BMRs fall into this category (Sreedevi et al. 2023).

The AutoTAB catalog includes the tracking information for all BMRs and their physical parameters, such as maximum magnetic field (B_{\max}), average magnetic field (B_{mean}), total unsigned flux (Φ_m), tilt (γ), as well as positional information (latitude λ and longitude ϕ), at each instance during their lifetimes. The tilt of a BMR is calculated similarly to that in Stenflo & Kosovichev (2012) and Jha et al. (2020), which varies between $\pm 90^\circ$. The convention followed here is that the BMRs, which strictly follow Joy’s law, have a positive tilt in the northern hemisphere, whereas it is negative in the southern hemisphere. Furthermore, the tilt of the BMRs emerging in the southern hemisphere is multiplied by a factor of -1 to match the tilts of the northern hemisphere, assuming hemispheric symmetry in tilt distribution. This convention is followed throughout the analysis.

3.1. Assigning Physical Parameters to BMRs

In most of the previous studies, every observation of a BMR has been treated as a new BMR. However, since the AutoTAB catalog provides the tracking information, we need to find a way to study the statistical properties of BMRs by assigning a unique number for BMR parameters. Thus, to get the single representative parameter for LT class BMRs, we picked the time period during which the measured Φ_m exceeds 80% of its

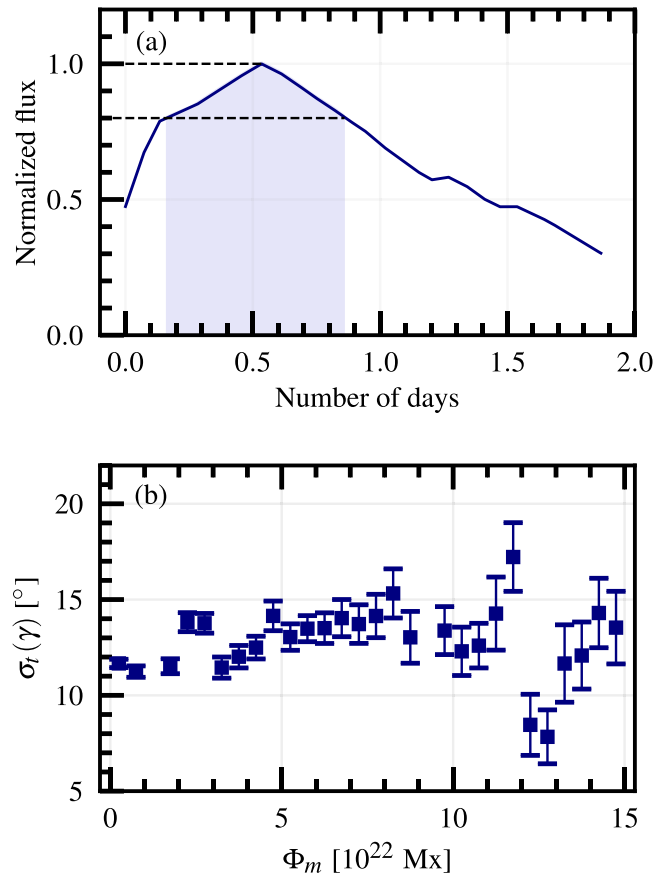


Figure 1. (a) Evolution of magnetic flux (Φ_m) of a representative BMR tracked by AutoTAB. The shaded area indicates the duration during which the measured Φ_m is greater than 80% of the maximum Φ_m recorded for the BMR. (b) Mean of the standard deviation of BMR tilt, $\sigma_t(\gamma)$ in each 5×10^{21} Mx flux bin plotted against Φ_m of the DP class BMRs.

maximum value during tracking. Following that, we calculate the average properties only during that period. To avoid projection effects, the maximum flux Φ_m of a BMR is considered only when it resides within 55° east–west. In Figure 1(a), we illustrate the evolution of flux of a typical BMR from the AutoTAB catalog. Here, the shaded region represents the time window when Φ_m is more than 80% of maximum Φ_m , and thus, the physical parameters (B_{mean} , B_{\max} , Φ_m , γ , and λ) are obtained by averaging over this time window.

Using this approach, we can easily assign a single value of a physical parameter for the LT class BMRs. However, assigning a single value to a BMR in the DP class, may not be appropriate as they are tracked at different evolutionary stages, and we may not have the maximum Φ_m during this period. For the tilt angle, it may be more questionable to assign a single value, as the fluctuations in the tilt are more pronounced compared to other parameters (refer to Figures 9 and 10 for case studies).

To gauge these fluctuations in tilt angles over BMR’s tracking period, we calculate the standard deviation $\sigma_t(\gamma)$ in tilt for a BMR over its lifetime for all the DP class BMRs. The variation of the mean of $\sigma_t(\gamma)$ in each flux bin of 10^{22} Mx is presented as a function of Φ_m in Figure 1(b).

While the fluctuation in the measured tilt over the tracked lifetime ($\sigma_t(\gamma)$) is even larger than the mean tilt, the trend in this figure suggests a relatively stable variation with respect to the flux. We, however, observe a potential decrease in $\sigma_t(\gamma)$ for

⁷ The time period for which AutoTAB tracks the BMR.

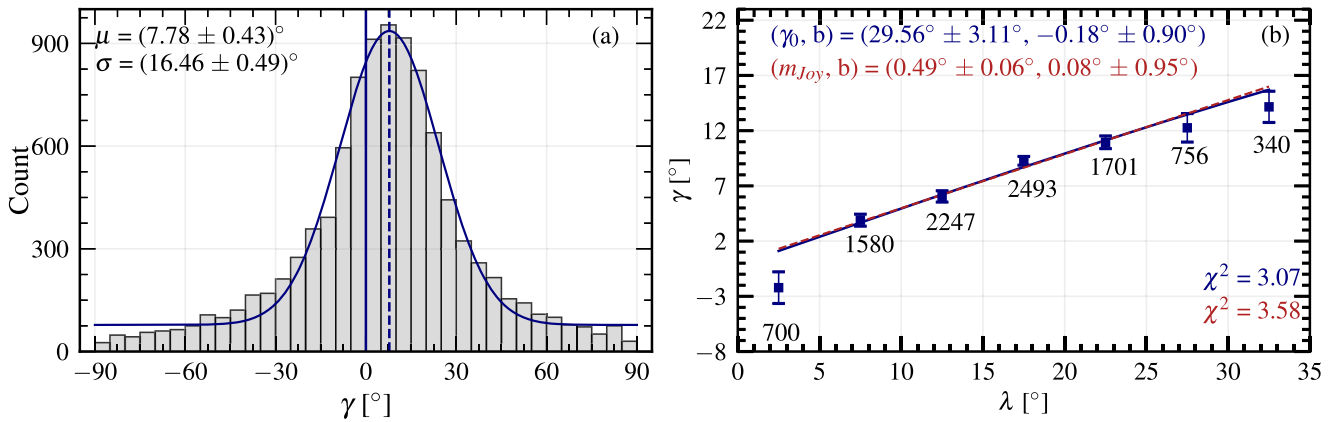


Figure 2. (a) Tilt distribution: number of BMRs in 5° tilt bins are shown as bars. The blue solid line represents the Gaussian fitted curve (with an offset) with fitting parameters mentioned in the panel. The vertical solid blue line represents the 0° tilt, and the blue-dashed line represents the Gaussian fitted mean at 7.78° . (b) (Gaussian) Mean tilt in each 5° latitude bin as a function of the latitude. Blue solid and red-dashed lines represent Joy’s law ($\gamma = \gamma_0 \sin \lambda + b$), and the straight line fits ($\gamma = m_{\text{Joy}} \lambda + b$) with fitting parameters mentioned in the panel along with the χ^2 value for the fit shown in the bottom right. The numbers appearing below the points display the total number of BMRs in the associated bins.

higher flux BMRs. The larger error bars at higher flux ranges result from a smaller number of BMRs in these bins. Hence, in this study, DP class BMRs can be uniformly analyzed and the same method for assigning the parameter values for the LT class can be followed for the DP class as well.

Figure 1(b) also suggests that BMRs having higher flux are less affected by convective buffeting, possibly due to quenched convection around them and a larger amount of magnetic tension; more on this will be discussed in Sections 4.2.4 and 4.2.5.

After outlining the method for assigning representative values to each tracked BMR, we proceed to assess the statistical behavior of BMRs.

4. Results and Discussion

4.1. Statistical Properties of Tracked BMRs

We start validating the AutoTAB catalog by studying its statistical properties and comparing them with the anticipated collective behaviors of BMRs based on previous studies (e.g., Howard 1991, 1996; Sivaraman et al. 2007). This serves as a preliminary step before investigating the observational signature for the thin flux tube model.

4.1.1. Distribution of Tilt

One of the best-known properties of tilt is its distribution. Hence, we start by evaluating whether the assigned tilts of BMRs show a familiar distribution, as observed in earlier studies by Wang & Sheeley (1991), Dasi-Espuig et al. (2010), and many others. In Figure 2(a), we show the distribution of tilts for all the BMRs from all latitudes. From this figure, we note that the tilt shows the well-known Gaussian distribution as reported in earlier works. The least-squares fit to the distribution with the Gaussian function (shown by the blue solid line in Figure 2(a)) gives a mean (μ) of 7.78° and a standard deviation (σ) of 16.46° . These values closely align with those obtained by Jha et al. (2020), where they did not track BMRs and treated each detection as an independent measurement. We also compared our distribution with that in Stenflo & Kosovichev (2012) by only considering BMRs in the latitude range of 15° – 20° in both hemispheres, and we find $\mu = 9.27^\circ$ and $\sigma = 14.90^\circ$, which show an excellent agreement.

We further analyzed the tilt distribution for individual cycles (Cycles 23 and 24) and separately for each hemisphere, and the fitting parameters are presented in Table 1. The μ and σ values obtained do not show a significant variation. Therefore, for our analyses, we combined the data from two hemispheres.

4.1.2. Joy’s Law

Another well-known property of BMRs is that they show a systematic dependence on latitude, i.e., Joy’s law. Therefore, we plotted the mean tilts of BMRs in each 5° latitude bin by folding both hemispheres; see Figure 2(b). Here, we calculate the mean by fitting a Gaussian function in the distribution of tilt in each latitude bin.

We fit these mean values with the standard Joy’s law function, i.e., $\gamma = \gamma_0 \sin \lambda + b$, (blue solid line), which yields a Joy’s law slope of γ_0 of 29.56 ± 3.11 , in agreement with previous reports (Stenflo & Kosovichev 2012; Jha et al. 2020). If we force the line to pass through the origin (i.e., $b = 0$), the γ_0 is modified to 28.98 ± 3.10 .

Sometimes, instead of sinusoidal dependence, a linear dependence ($\gamma = m_{\text{Joy}} \lambda + b$) is also used for the tilt–latitude relation (e.g., Wang & Sheeley 1991; Sivaraman et al. 1999). In Figure 2(b), we also fit the mean γ with this linear fit, which is shown by the blue-dashed line (almost on top of the red-dashed line). The slope of the fitted line is 0.49 when $b \neq 0$ and 0.50 when $b = 0$. These values are significantly higher than the previously reported values of 0.26 and 0.28, based on white-light observations at Mount Wilson and Kodaikanal Observatories, respectively (Dasi-Espuig et al. 2010). One reason behind this discrepancy is the difference in data type, as the magnetogram tends to give a higher slope of Joy’s law than the white light (Wang et al. 2015). Since there is no significant difference between the fitted lines in Figure 2(b), we use the sinusoidal dependence as the standard Joy’s law.

4.1.3. Flux versus Magnetic Field

Assigned B_{max} and Φ_m values of the tracking data from AutoTAB reveal a correlation between them, depicted in a scatter plot of Figure 3. The (Pearson) correlation coefficient between the quantities is 0.72, suggesting a good correlation between B_{max} and Φ_m . A similar trend (not shown) is observed

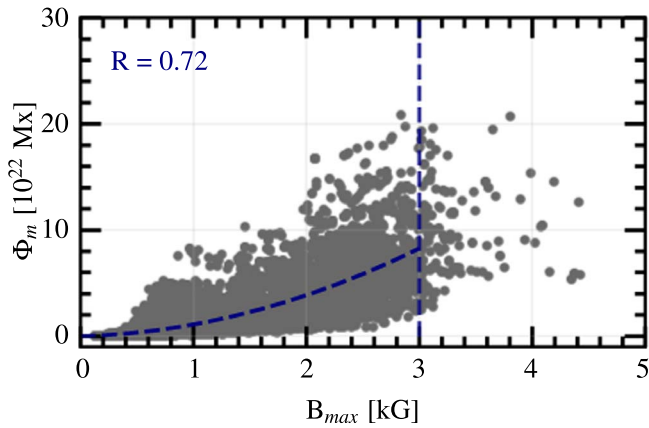


Figure 3. Scatter plot between the measured B_{\max} and Φ_m . The blue-dashed line represents the quadratic fit (see the text). Flux values are capped at 3×10^{23} Mx, and the outliers beyond this range are attributed to the effects of defective pixels and faulty detection.

Table 1
Fitting Parameters of the Tilt Distribution for Different Cycles and Hemispheres

Cycle	Hemisphere	μ (deg)	σ (deg)
Cycle 23	North	7.72 ± 0.59	15.76 ± 0.67
	South	7.17 ± 0.45	16.76 ± 0.52
	Combined	7.42 ± 0.42	16.32 ± 0.48
Cycle 24	North	8.52 ± 0.56	16.16 ± 0.63
	South	7.13 ± 0.40	17.13 ± 0.46
	Combined	7.55 ± 0.55	16.92 ± 0.64

between B_{mean} and Φ_m as well. It is important to note that the measured B_{\max} values are affected by the saturation limit of MDI and HMI, but the saturation effects will not significantly influence the measurement of Φ_m of the regions (Hoeksema et al. 2014). Therefore, the observed stabilization of B_{\max} with Φ_m beyond B_{\max} of 3 kG in Figure 3 may reflect this phenomenon, and measurements in high-field regions will be significantly constrained by the saturation of the instrument. The quadratic fit is slightly better, and the relation becomes B_{\max} below 3 kG and is given by $B_{\max} = (0.83 \pm 0.02)\Phi_m^2 + (0.27 \pm 0.04)\Phi_m$. (If we fit with a cubic relation, then the equation reads as $B_{\max} = (0.08 \pm 0.03)\Phi_m^3 + (0.56 \pm 0.1)\Phi_m^2 + (0.48 \pm 0.09)\Phi_m$.) The cutoff of 3 kG is set to address the saturation of the instrument. Given this limitation, the relation in Figure 3 suggests stronger BMRs are associated with higher magnetic flux.

4.2. Validation of the Thin Flux Tube Model

After discussing the collective behaviors of the tracked regions, in this section, we delve into an examination of whether the tracked information from AutoTAB aligns with the expected outcomes proposed by the thin flux tube model, as discussed in Section 2.

4.2.1. Evolution of Footpoint Separation of BMRs

To assess the validity of the rising flux tube model, i.e., the rise of Ω loop, we calculate footpoint separation (D) at each time step of observation throughout the lifetime of the LT class BMRs. Here, D is defined as the angular distance between the two polarities of the BMR at each instance of the tracking of a

BMR calculated using

$$D = R_{\odot} \cos^{-1} [\cos \lambda_1 \cos \lambda_2 \cos(\phi_2 - \phi_1) + \sin \lambda_1 \sin \lambda_2]. \quad (2)$$

The heliographic location of the polarities is calculated based on the flux density-weighted mean location of BMR's polarity. In Figure 4(a), we show the footpoint separation (D) of BMR polarities as a function of time, normalized by their lifetimes, to bring them on the same footing.

In Figure 4(a), we can see a steady, rapid increase in D during the initial phase of the evolution of the BMRs, followed by a slow increase in the later stage. However, the evolution of D of a typical BMR, shown in Figure 1 of Kosovichev & Stenflo (2008), depicts a downward trend in the footpoint separation toward the disintegration phase of the BMR, which is not evident in Figure 4(a). To further explore the behavior observed by Kosovichev & Stenflo (2008), we look at a few individual BMRs (Figure 9 in the Appendix). We observe that in some cases, there is indeed a downward trend in D toward the later phase of the BMR lifetime (see Figure 10(a), (f), (g), (i), (k)). However, we find a statistically consistent increase in D along with saturation in the later part of the BMR's lifetime, which aligns with the expectation of the rise of Ω -shaped flux tube.

A closer inspection of Figure 4(a) shows a rapid increase in the footpoint separation occurs during the initial phase (5%–30% of lifetime). This accelerated growth phase in BMR evolution was previously reported as Phase 1 (acceleration) by Schunker et al. (2019). The rate of the rise in footpoint separation slows down in the later phase, suggesting that this could be Phase 2 (deceleration), as suggested by Schunker et al. (2019). To further investigate this behavior, we segregate the BMRs into three different flux ranges based on the assigned flux, Bin I: 10^{20} – 10^{21} Mx, Bin II: 10^{21} – 10^{22} Mx, and Bin III: 10^{22} – 10^{23} Mx, and we study the evolution of D and the major contributors to D , i.e., $\Delta\phi$, and $\Delta\lambda$ in each of the flux bins shown in Figure 4(b)–(d), respectively. Figure 4(b) represents the evolution of D in various flux bins. The increase in D observed in Figure 4(a) is primarily contributed by Bin II, and the trend also suggests that higher flux regions are associated with higher D , which is consistent with previous findings (Schunker et al. 2019). The evolution of $\Delta\phi$ shown in panel (c) reflects the rapid increase seen in D in higher flux ranges (Bin II and Bin III); however, in Figure 4(d), such a trend is not evident in the evolution of $\Delta\lambda$. We also would like to point out that the trend depicted in Figure 4(a) persists across the latitudinal bins, with their patterns overlapping.

It has been suggested in previous simulation studies by D'Silva & Choudhuri (1993), Schüssler & Rempel (2005) that the flux tubes get tethered from the CZ as they rise up. If the tethering happens, the reflection of the same can be seen as a rapid change in longitudinal separation and a steady change in latitudinal separation, due to imparted circular motion from the twisted flux tubes. Now, the question arises, “When does the tethering happen in a flux tube?” One can assume that flux tubes with lower strength and lower flux content will tether from the CZ at an earlier time compared to stronger flux tubes.

The rapid change in $\Delta\phi$ in the higher flux bins shown in Figure 4(c) may be attributed to this effect. However, we fail to find any statistically significant variation in $\Delta\lambda$ in Figure 4(d). An important consideration here is that the BMRs in LOS magnetogram data are detected only once the flux tubes emerge

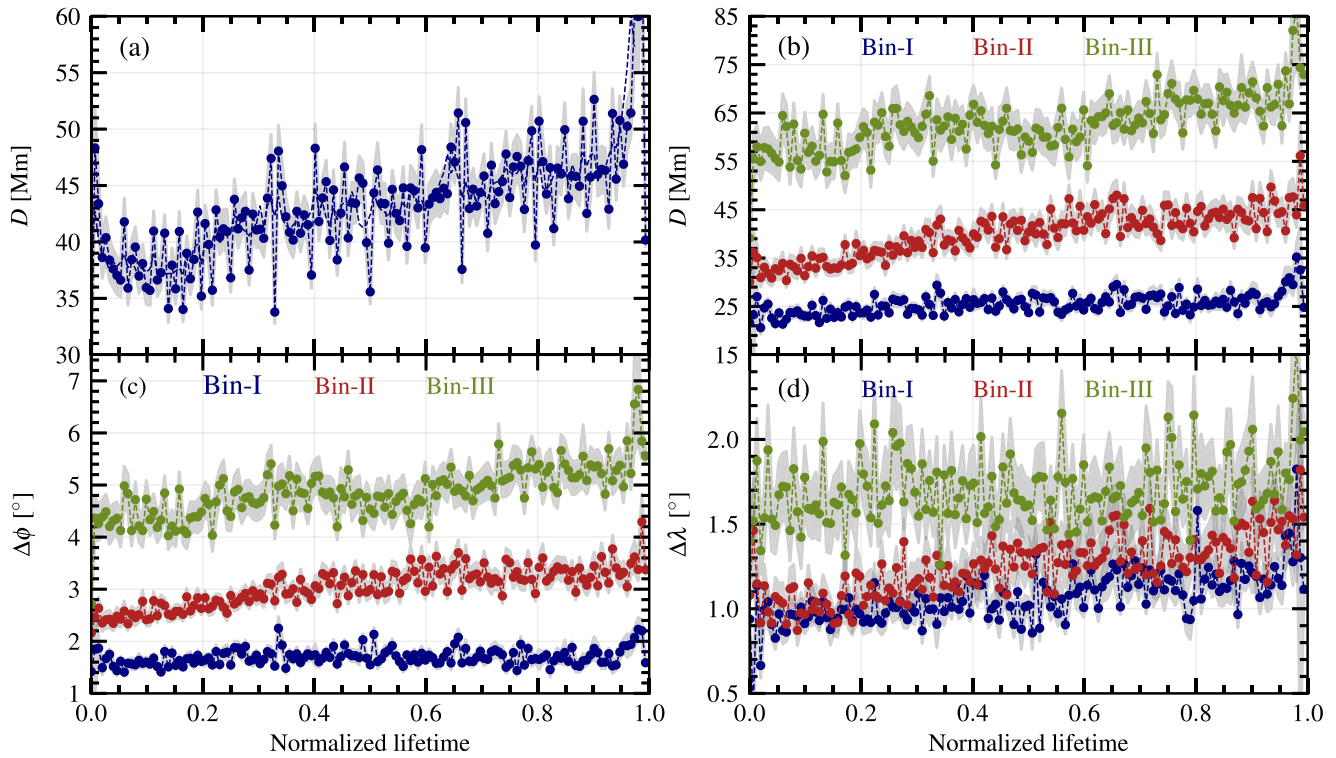


Figure 4. (a) General evolutions of footpoint separation of BMR (D) over its lifetime. (b) Shows the same but in three different flux ranges: Bin I: 10^{20} – 10^{21} Mx (blue), Bin II: 10^{21} – 10^{22} Mx (red), and Bin III: 10^{22} – 10^{23} Mx (green). (c) and (d) show the same as in (b) but for the longitudinal separation ($\Delta\phi$) and latitudinal separation ($\Delta\lambda$), respectively. Note that the time is normalized to their lifetimes, and the quantities (D , $\Delta\phi$, and $\Delta\lambda$) are averaged over all BMRs in each 96 minute cadence.

from the photosphere radially. Additionally, AutoTAB tracks them exclusively when both polarities have emerged, and they hold a strong flux balance condition. Hence, the data set lacks information about the onset of the emergence phase of the BMR. The absence of a rapid increase in lower flux regions could be because tethering had already occurred before AutoTAB started tracking the BMRs. This is in contrast to higher flux regions, where tethering occurs at a later stage, allowing AutoTAB to track them during the tethering period effectively and reflected as the rapid increase in $\Delta\phi$, as can be seen in Figure 4(c).

4.2.2. Tilt Angle at the First Detection

The evolution of D lends support to the assumption of ascending flux tubes associated with the formation of BMRs. One debated point has been whether the BMRs emerge with a definite tilt, or they acquire the observed tilt after emergence. According to the thin flux tube model, BMRs should have acquired tilt as the flux tubes rise through the CZ. Hence, we anticipate a definite tilt angle in BMRs at the emergence. To evaluate this, we collected all those BMRs that emerged on the nearside of the Sun and looked for their tilt and Joy’s law behavior at the very first detection. We emphasize that the latitude and tilt values considered here correspond to the first detection of the BMR. To avoid the projection effect, we restrict the BMR emergence between 45° east and west longitudes. AutoTAB tracks 5635 such BMRs, which lie within the flux range of 10^{19} – 10^{23} Mx with the median at 4.05×10^{21} Mx.

In Figure 5, first, we plot the Gaussian mean in each latitude bin of 5° and then fit the Joy’s law function using the least-squares fitting method. Here, we note that the BMRs show a

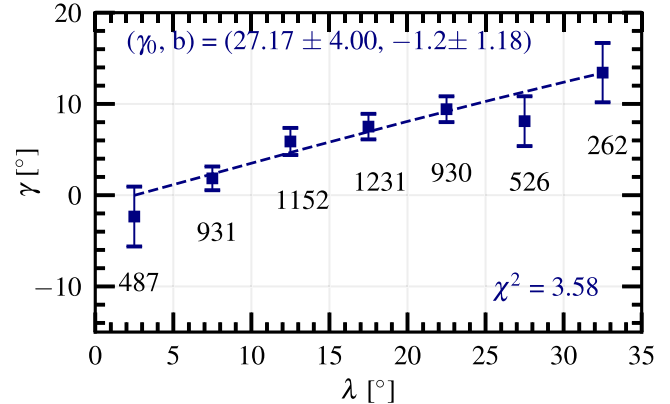


Figure 5. Joy’s law plot at the first detection of the BMR emerging between 45° east-west. (Gaussian) Mean tilt in each 5° latitude bin as a function of the latitude. Blue-dashed lines represent Joy’s law fit ($\gamma = \gamma_0 \sin \lambda + b$) with the parameters and χ^2 value for the fit shown in the panel. Numbers appearing below the points mark the total number of BMRs in the associated bins.

definite tilt at their first detection, which increases with latitude, as we expect from Joy’s law. However, Joy’s law’s amplitude of $\gamma_0 = 27.17$ implies a somewhat weaker dependence on latitude compared to that shown in Figure 2(b). Comparing this γ_0 with that obtained during the mature phases, we find that the tilt increases in the later phase of the BMR’s life, which is consistent with previous findings (Kosovichev & Stenflo 2008; Schunker et al. 2019). This is also visible in the individual case studies shown in Figure 10. Nevertheless, based on the behavior observed in Figure 5, we can say that, statistically, BMRs emerge with a definite tilt in accordance with Joy’s law.

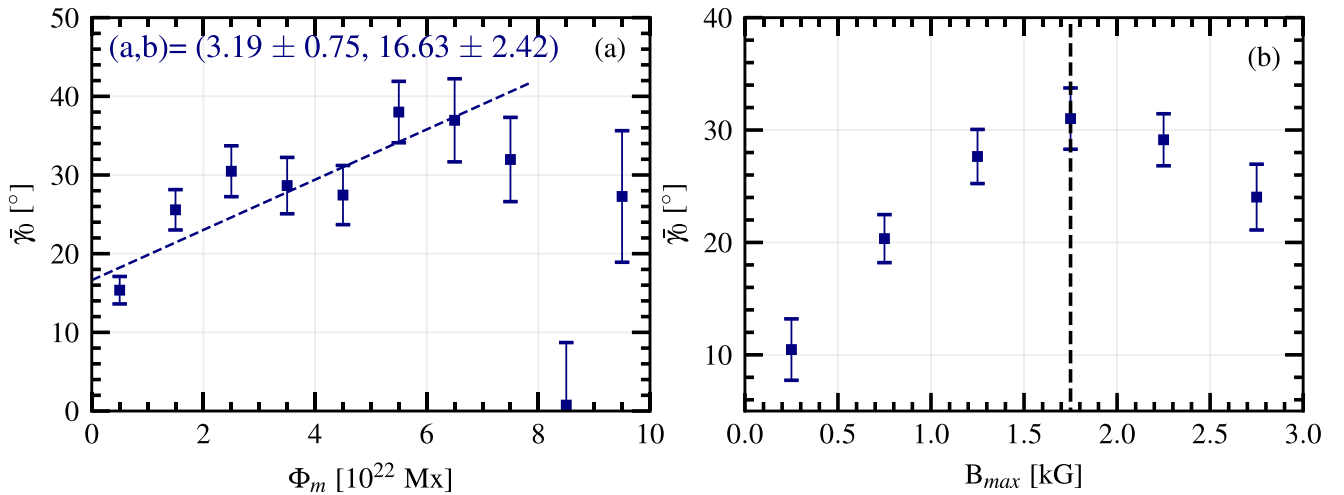


Figure 6. (a) Mean $\overline{\gamma}_0$ is calculated in each flux bin (Φ_m) of length 1×10^{22} Mx and is plotted as a function of Φ_m . The blue-dashed line represents the straight line fit ($\overline{\gamma}_0 = a\Phi_m + b$), excluding the last two points with parameters shown at the top of the panel. Here, the error bars represent the standard error in each flux bin, which is bigger in the high-flux bins because of a smaller number of BMRs. (b) Mean $\overline{\gamma}_0$ is calculated in each B_{\max} bin of length 0.5 kG and is plotted against B_{\max} . The vertical black-dashed line represents B_{\max} at 1.75 kG.

Schunker et al. (2019, 2020) suggested that BMRs emerge with zero tilt and develop tilt in accordance with Joy’s law in the later part of their lifetimes from the analysis of the Solar Dynamic Observatory Helioseismic Emerging Active Region survey, thereby arguably ruling out the Coriolis force as a possible cause of the tilt in the BMRs. The active regions chosen for their study mainly had two criteria: (i) The regions should appear in the continuum observation, and (ii) regions should emerge in the quiet Sun region and not in a region close to an existing active region. We argue that these criteria may lead to selection bias, and the result may be affected by this. To validate if the BMR emerges with zero tilt or not, we conducted some case studies of the BMR. We remind that AutoTAB tracks the BMR only for the time period in which the flux balance condition holds, and the initial developing signatures of BMRs might have been missed in the tracking. Therefore, we select some BMRs at various stages of solar cycles and flux ranges and go back in time (time before they were detected by AutoTAB) to observe their tilt at the emergence phase. While making our selection, we make sure that the latitude of the emergence of these BMRs is between $\pm 30^\circ$ and with no prominent flux emergence nearby. Snapshots of 12 such BMRs and their evolutions are shown in Figure 9, along with the evolution of Φ , γ , and D shown in Figure 10. Our observations based on these selected BMRs reveal that eight of them emerge with a definite tilt, while the remaining emerge with nearly zero tilt. Furthermore, we also note that the BMR signatures emerging with or without tilt do not depend on the latitude of their emergence, the time it takes to be detected by AutoTAB, or their flux strength. The factors determining a BMR emerging with or without tilt remain unclear and require further exploration. Nevertheless, it is noted that the nearby emergence of flux can influence the tilt of the emerging BMRs.

In summary, as observed in case studies and based on Figure 5, we confirm that the Joy’s law trend is clearly evident at the first tracking detection. This suggests that some tilt is imparted to the BMRs below the surface before they are observed in the magnetograms, and the major cause of the BMR tilt could be the Coriolis force.

4.2.3. Flux Dependence of Tilt

As the BMR flux is observed to show a wide variation in magnitude (more than 3 orders), we expect to detect a variation of tilt with the magnetic flux, which was one of the predictions of the thin flux tube model, as discussed in Section 2. To assess the dependence of tilt on flux, we compute $\overline{\gamma}_0 = \langle \gamma \rangle / \langle \sin \lambda \rangle$ in each 10^{22} Mx flux bin and plot them against the Φ_m shown in Figure 6(a). We note that in computing $\overline{\gamma}_0$, a normalization factor $\langle \sin \lambda \rangle$ is used to get rid of the latitudinal dependency in Joy’s law. However, this quantity, $\overline{\gamma}_0$, is strictly not the slope of Joy’s law (γ_0). Taking the average on both sides of Equation (1), we can regard this factor $\overline{\gamma}_0$ as the mean slope of Joy’s law. Instead of computing it in this way, if we compute γ_0 in the traditional method (i.e., by fitting tilt versus latitude variation) in each flux bin, then we get a statistically insignificant value of γ_0 , due to limited data in some bins (however, see the next section). Despite this, we observe a consistent increase in $\overline{\gamma}_0$ with Φ_m until 7×10^{22} Mx, and the best fit is found to be linear ($\overline{\gamma}_0 = a\Phi_m + b$).

This dependence is much stronger than the one predicted by the thin flux tube model of Fan et al. (1994); see Equation (1). However, we note that the measured total unsigned flux of the BMR might be an averaged representation of flux inside the tube, and a precise simulation-like behavior cannot be anticipated from observational data. Nevertheless, any observed dependence of $\overline{\gamma}_0$ on Φ_m indicates a significant dependence of tilt on the flux of the BMR and thus supports the thin flux tube model.

After 7×10^{22} Mx, we observe an indication of a decrease of $\overline{\gamma}_0$ with Φ_m (assuming that there is no saturation limit in the measurements). The reliability of these data points in the graph is, however, compromised, due to the limited number of high-flux BMRs. Nevertheless, this decrease could be due to the dominant effect of the magnetic field at a large flux (as B_{\max} increases with Φ_m ; Figure 3). While the tilt increases with the magnetic flux, it decreases with the field in the flux tube; see Equation (1). In the high-flux regime, the effect of the magnetic field dominates over the flux and causes a decrease in the tilt. This decrease in tilt is referred to as tilt quenching by Jha et al. (2020; also see the inclusion of tilt quenching in dynamo

models by Karak & Miesch (2017, 2018), who observed a decrease in γ_0 with B_{\max} (see Figure 4(a) in Jha et al. 2020). In our tracked BMR data, we also find a similar trend between B_{\max} and $\overline{\gamma_0}$, as observed by Jha et al. (2020), with an initial increase in γ_0 with B_{\max} followed by a mild descent beyond 1.75 kG. However, the reliability of the data points for higher B_{\max} bins is limited for the same reasons, as highlighted in Section 4.1.3 (saturation limit in measurements).

The trends shown in Figure 6 indicate a dynamic interplay of forces on rising flux tubes. Small and moderate field and flux might represent a region where the drag and Coriolis forces dominate over the magnetic buoyancy, while the regime with $B_{\max} > 1.75$ kG (and $\Phi_m \gtrsim 7 \times 10^{22}$ Mx) represents the magnetic buoyancy-dominated regime, resulting in reduced tilt.

4.2.4. Flux Dependence of Joy's Law

To further explore the magnetic flux dependence of tilt, here we revisit Joy's law. We have seen in Figure 2(b) that the tracked BMRs from the AutoTAB catalog collectively obey Joy's law. However, we have already noted that the tilt data is extremely noisy (e.g., Figure 1(b)), and Joy's law trend is evident only after averaging. A possible contribution to the scatter in the tilt is due to the turbulent convection affecting the flux tube as it rises through the CZ (e.g., Longcope & Choudhuri 2002; Weber et al. 2013), and thus, the effect of scatter is more prominent in lower flux bins. We have already seen some evidence of it as shown in Figure 1(b). We, therefore, segregate the BMRs into three bins with an equal number of data points in each bin. To keep the same number of data points in each bin, the flux ranges in these bins become 1.72×10^{19} – 3.13×10^{21} Mx (Bin I), 3.13×10^{21} – 2.38×10^{22} Mx (Bin II), and 2.38×10^{22} – 9.92×10^{24} Mx (Bin III). We note that although the maximum flux of BMR in Bin III goes to a very large value, there are only a few BMRs above 2×10^{23} Mx; see Figure 3. (In fact, the median flux values in each bin are 6.64×10^{20} Mx, 9.81×10^{21} Mx, and 5.28×10^{22} Mx, respectively.) Figure 7 displays tilt as a function of latitude, along with the Joy's law fit, for the BMRs in these bins. We observe that as we move to the higher flux regimes (Bins II and III), the scatter decreases, which agrees with the theoretical expectation that the stronger BMRs are less buffeted by convection.

Also, seeing a large scatter around Joy's law and a large error in the fitted parameters in Bin I, having the BMR flux $< 3.13 \times 10^{21}$ Mx, we raise doubt about whether Joy's law behavior is valid only for stronger BMRs. Interestingly, if we discard this bin, then from panels (b) and (c), we can observe that the slope of Joy's law γ_0 increases as we move from Bin II (having mean flux 1.11×10^{22} Mx) to Bin III (mean flux 4.93×10^{23} Mx). This increase in γ_0 is in agreement with the theoretical prediction, and in particular, with the result presented in the previous section (Section 4.2.3) that $\overline{\gamma_0} = \langle \gamma \rangle / \langle \sin \lambda \rangle$ increases with flux.

We note that as shown in Figure 7, the result also remains consistent if we include only the BMRs within the flux range of 10^{20} – 10^{23} Mx (i.e., if we cut out the two tails of the flux distributions) and bin the data in equal numbers. Interestingly, if we bin the data in equal flux bins such that the flux ranges become 10^{20} – 10^{21} Mx (Bin I), 10^{21} – 10^{22} Mx (Bin II), and 10^{22} – 10^{23} Mx (Bin III), then the value of γ_0 in Bin II and Bin III are comparable. However, the decrease in scatter from Bin I to Bin II remains consistent in this case as well. This suggests

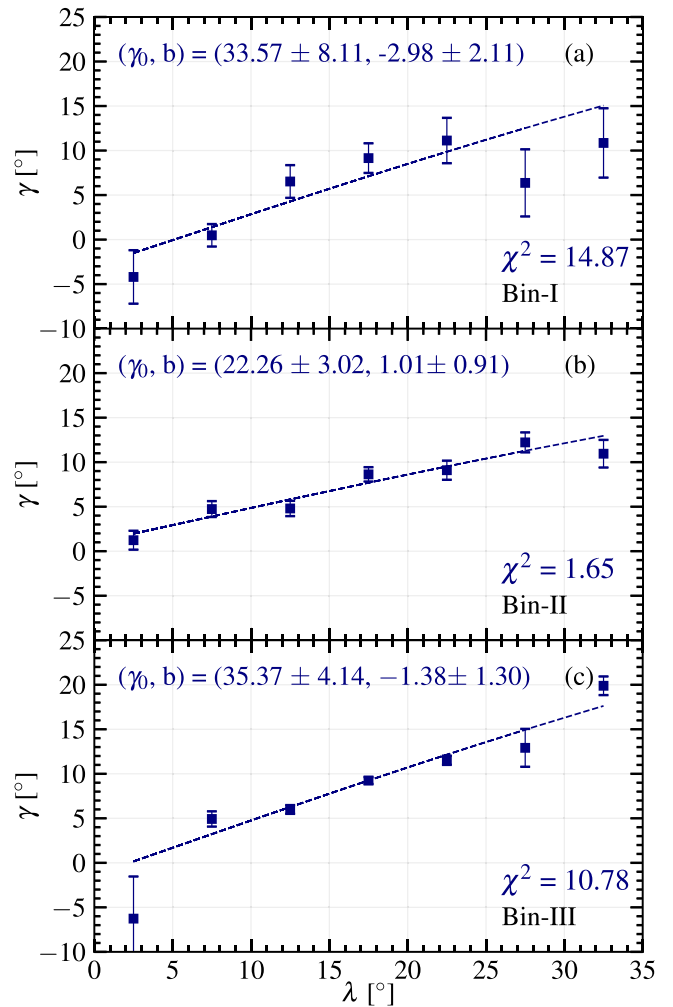


Figure 7. Joy's law dependence for BMRs with flux (a) Bin I (1.72×10^{19} – 3.13×10^{21} Mx), (b) Bin II (3.13×10^{21} – 2.38×10^{22} Mx), and (c) Bin III (2.38×10^{22} – 9.92×10^{24} Mx). The blue-dashed line represents the Joy's law fit of $\gamma = \gamma_0 \sin \lambda + b$ with fitting parameters mentioned on the panel in blue.

that Joy's law fitting is sensitive to how we bin the data points. This could be why previous authors could not find a systematic increase in γ_0 with the flux (Kosovichev & Stenflo 2008; Stenflo & Kosovichev 2012). Therefore, $\langle \gamma \rangle / \langle \sin \lambda \rangle$ may be a better quantity when measuring the flux dependence of BMR tilt as done in Section 4.2.3.

4.2.5. Variation of Tilt Fluctuations with Footpoint Separation

Based on the thin flux tube model, it is expected that as the tubes rise through CZ, they are buffeted by convection. Including turbulence in the numerical model of a thin flux tube, Longcope & Fisher (1996) predicted the dependence of the tilt angle fluctuations i.e., the rms value of the tilt $\text{rms}(\gamma)$ with the footpoint separation D . They showed that as D increases, (i) the averaging effect of small-scale wiggles over the flux tube is greater, leading to a straight rise of the tube and (ii) the flux increases, which consequently decreases the rise time or the time for the interaction with convection. They showed that $\text{rms}(\gamma)$ scales as $1/D$. We investigate this behavior by showing the variation of $\text{rms}(\gamma)$ with D from the AutoTAB catalog as shown in Figure 8. We observe that $\text{rms}(\gamma)$ decreases with increasing footpoint separation exactly as reported by Longcope & Fisher (1996; $\text{RMS}(\gamma) = a/D + b$). We note that from white-light

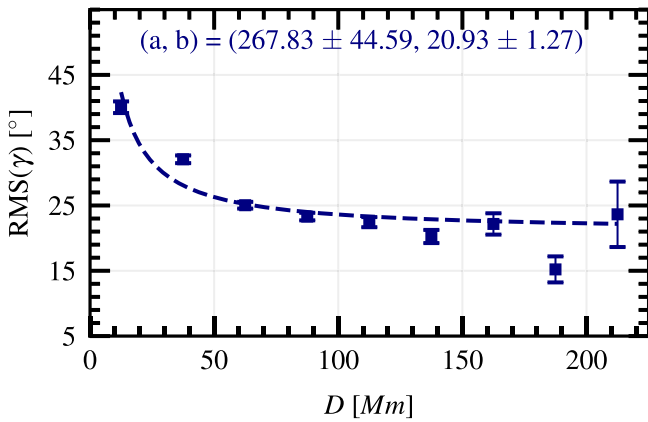


Figure 8. rms of the tilt ($\text{rms}(\gamma)$) calculated in each footpoint separation (D) bin of length 25 Mm and is plotted as a function of D .

observations, Fisher et al. (1995) also found a similar dependence: $\text{rms}(\gamma) \simeq 10^\circ(D/100)^{-3/4}$.

5. Conclusions

The thin flux tube model provides the simplest explanation for the formation of BMRs, postulating magnetically buoyant tubes anchored at the CZ. According to this model, the Coriolis force imparts tilt to the emerging BMRs. Despite its popularity, the theory lacks observational backing. This study undertakes an investigation into the validity of the model’s assumptions using the AutoTAB catalog.

AutoTAB is an in-house developed algorithm to automatically detect and track the BMRs from MDI (1996–2011) and HMI (2010–2023) LOS magnetogram data. The resulting comprehensive catalog documents the evolution of 12,173 BMRs on the nearside of the Sun. As a sanity test, we first assign a single representative value for BMR properties (B_{max} , B_{mean} , Φ_m , γ) by averaging their values during the times when their flux exceeds 80% of the peak values. We then show that BMRs follow (i) a Joy’s law trend ($\gamma_0 = 29^\circ.56$), (ii) Gaussian-like tilt distribution ($\mu = 7.78 \pm 0.43$), and (iii) magnetic flux versus field dependence. These are all consistent with previous studies. With these basic tests, we proceed with detailed analyses of our tracked BMRs to validate the thin flux tube model as a theory behind the BMR formation. The buoyant rise in the flux tube assumption is validated by examining the footpoint separation (D) over the BMR’s tracked lifetime. Our findings indicate a rapid increase in D during the initial phase of BMR evolutions, followed by a gradual rise and eventual saturation toward the end of their lifetime. The rapid increase is primarily attributed to the longitudinal separation ($\Delta\phi$), particularly pronounced in higher flux regions. This may imply a connection between rapid D growth and footpoint tethering from the CZ, where the immediate effect of the same manifests as a sudden increase in $\Delta\phi$.

In line with the thin flux tube model, BMRs are expected to appear with tilt at the onset of the emergence phase, due to the effect of Coriolis force during the rise of flux tubes. Our analysis of the Joy’s law trend in tracked BMRs of the LT class supports this expectation by demonstrating a clear Joy’s law trend in their first detection. This was further evaluated through case studies of individual BMRs selected from different phases of cycles and strengths. Our findings reveal a nuanced scenario, where the signatures of some BMRs emerge with zero tilt and develop at

later phases, while the rest exhibit a significant tilt from the beginning. This tilt behavior is independent of the emergence of latitude or cycle phase, indicating a potential contribution of the Coriolis force to a part of an observed tilt in BMRs.

Further, based on the thin flux tube model, we expect the tilt to increase with the increase of magnetic flux (D’Silva & Choudhuri 1993; Fan et al. 1994); also see Equation (1). We explored this flux dependence of tilt by computing $\overline{\gamma_0} = \langle \gamma \rangle / \langle \sin \lambda \rangle$. Our results reveal a linear increase in $\overline{\gamma_0}$ with Φ_m , signifying a pronounced tilt dependence on magnetic flux. A similar trend is observed concerning B_{max} , with an initial increase in $\overline{\gamma_0}$ for lower B_{max} regions, followed by a decrease after 1.75 kG. We further observed that the variation in Joy’s law is flux dependent. Joy’s law is less significant (and has a large scatter around the mean trend) at the small flux bin (below about 10^{21} Mx). The slope of Joy’s law increases as we move the BMR flux bin from 10^{21} to 10^{23} Mx. This result is again in agreement with the prediction of the thin flux tube model.

Finally, based on the thin flux tube model, we expect that the tilt fluctuation (rms value) will depend on the footpoint separation (e.g., Longcope & Fisher 1996). BMRs having large footpoint separation have less chance of being buffeted by the convection. From our data, we find that the tilt fluctuation decreases inversely with the footpoint separation as predicted by the model of Longcope & Fisher (1996).

Although our analysis provides some support to the thin flux tube model and hints at Coriolis force as the reason behind part of the tilt observed in the BMR, further study using richer data is needed to strengthen our conclusion. Notably, we have to carefully identify the emergence phase of a BMR and automatically compute the tilt of a large number of BMRs to check the statistical reliability of tilt at the very early phase of a BMR. We also need to explore the flux dependence of the tilt angle using a longer data set.

Acknowledgments

A.S. sincerely expresses gratitude to ARIES, Nainital, for the warm hospitality extended during the project’s initial phase. B.B.K. acknowledges the financial support from the Department of Science and Technology (SERB/DST), India, through the Ramanujan Fellowship (project No. SB/S2/RJN-017/2018) and the MATRICS grant (file No. MTR/2023/0000670). A.S. and B.B.K. thank Sami Solanki, Natalie Krivova, and Robert Cameron for their valuable comments and discussions during their visit to the Max Planck Institute for Solar System Research, Göttingen, which helped in improving the manuscript. The observational data, the LOS magnetograms from MDI and HMI, used in this article were obtained via JSOC, courtesy of the NASA/SOHO and NASA/SDO science teams.

Appendix Examples of Evolutions of BMRs

Panels (a)–(f) and (g)–(l) in Figure 9 present snapshots to illustrate the evolution of 12 distinct BMRs tracked by AutoTAB from Solar Cycle 23, starting from the point when the BMR signatures first emerged. The snapshots with red rectangles are produced from the times when AutoTAB could track the BMRs, while the snapshots with blue rectangles show their evolutions back in time. The criteria for region selection were as follows: (i) Individual BMRs’ emerging signatures

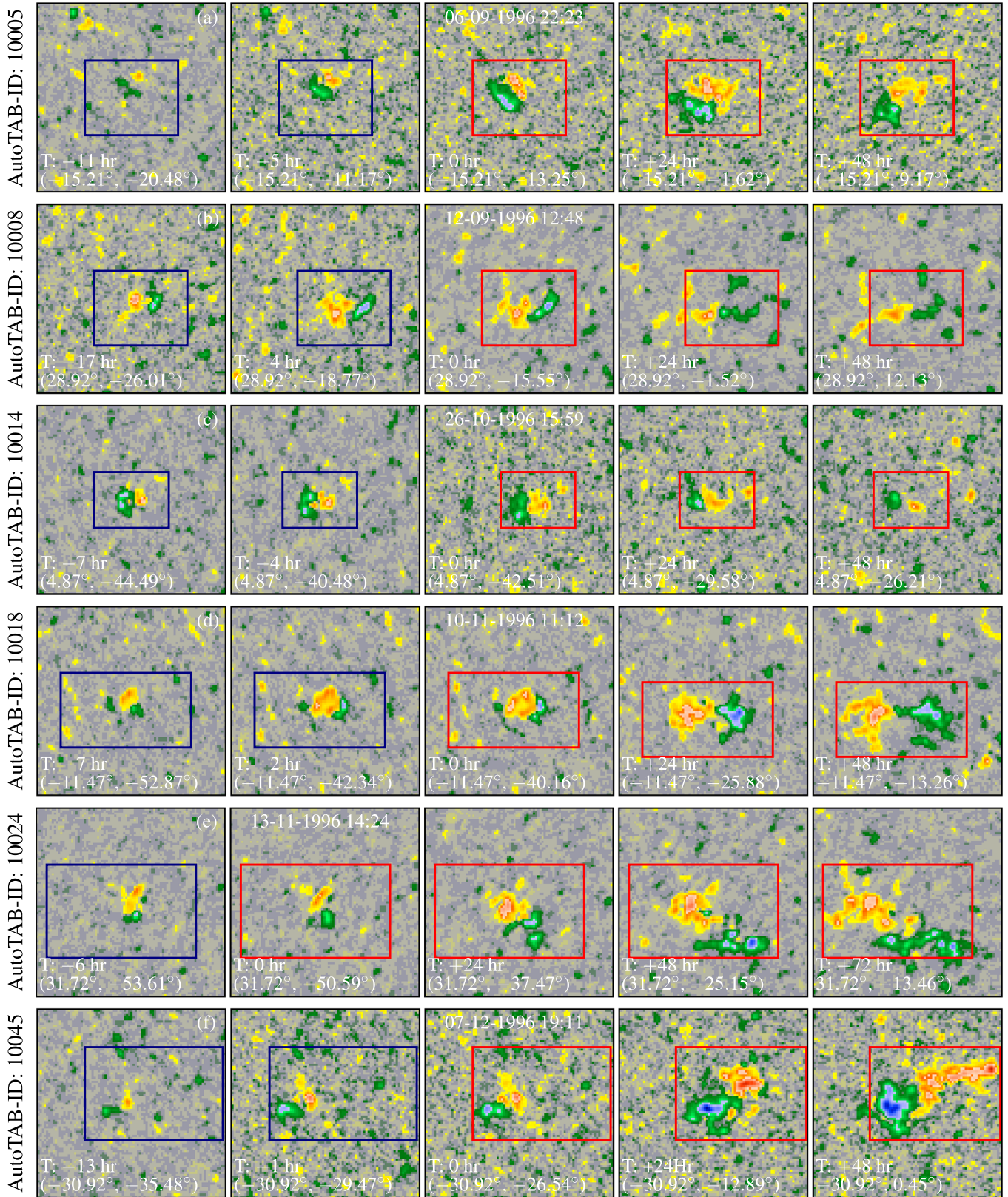


Figure 9. Snapshots of the evolution of 12 BMRs tracked by AutoTAB with a 1 day cadence. See the text for details. Numbers in the brackets at the bottom of the panels represent the mean latitude and longitude of the regions depicted.

should fall within $\pm 55^\circ$ longitude and $\pm 30^\circ$ latitude, and (ii) there should be no significant flux emergence in the vicinity. The “T” value at the bottom indicates the evolutionary stage of

the BMR. “T:0” signifies the initial detection by AutoTAB. Pre- and post-detection times are indicated in hours, denoted by negative and positive signs. The time and date of first detection

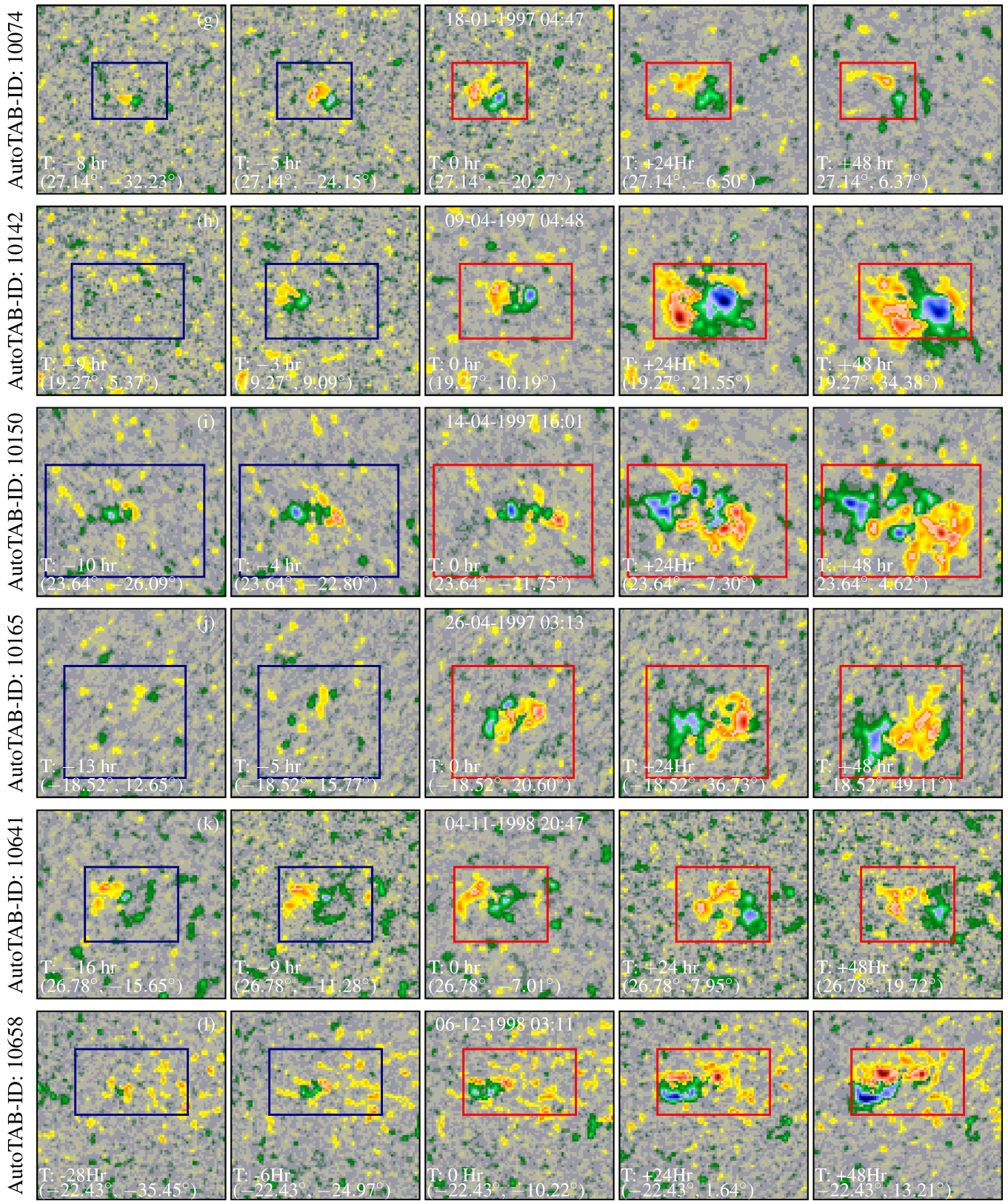


Figure 9. (Continued.)

are shown in the top of the panel of T:0. The bracketed numbers denote the mean heliographic latitude and longitude for each evolutionary stage.

Among the selected regions, we observed that eight BMRs emerged with a significant tilt at the initial phase itself, while others emerged with nearly zero tilt. The evolution of γ , Φ_m ,

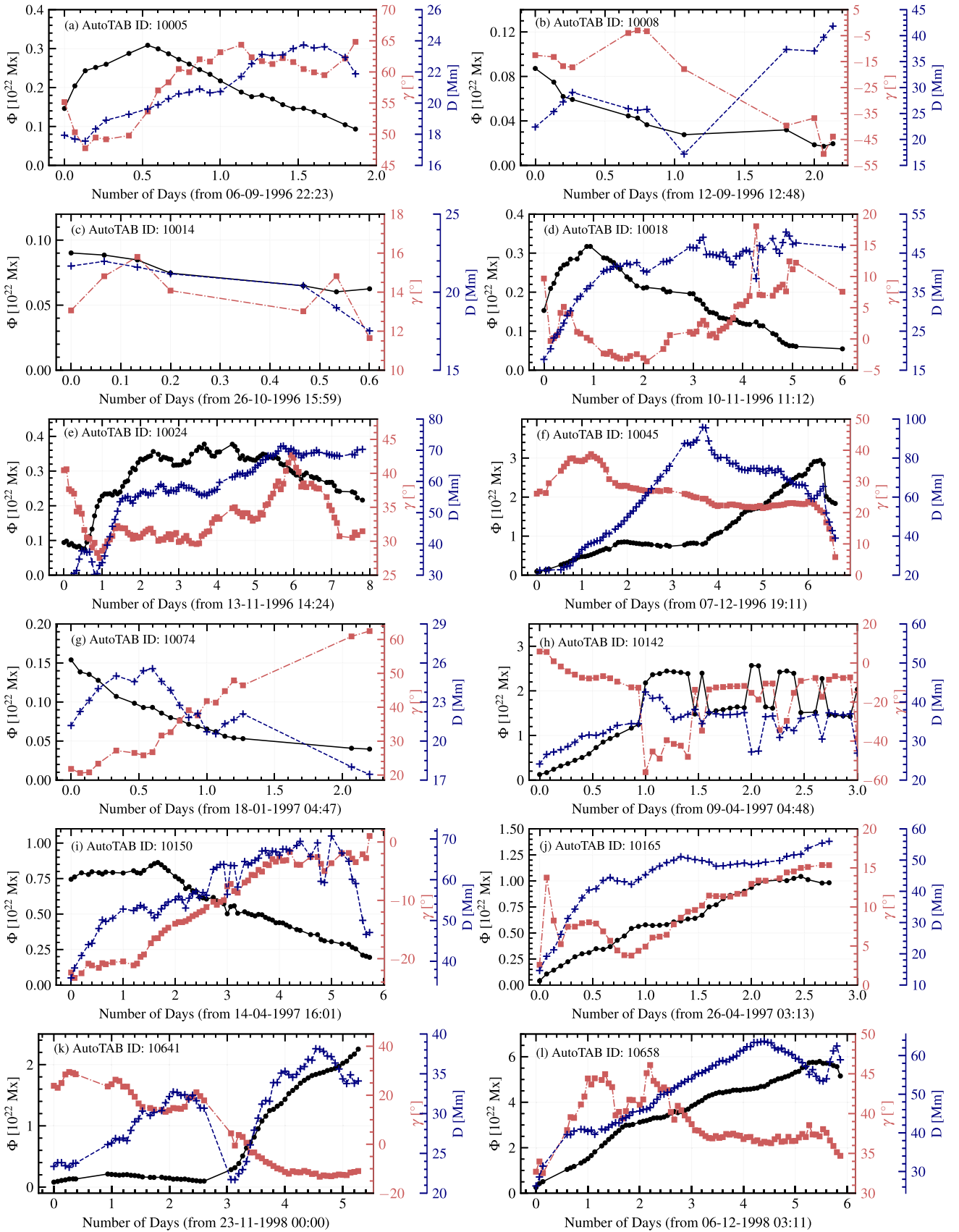






Figure 10. Time evolutions of flux, tilt, and footprint separation of 12 BMRs, whose evolution are shown in Figure 9.

and D during their tracked lifetimes for all the selected BMRs are illustrated in panels (a)–(l) in Figure 10.

ORCID iDs

Anu Sreedevi  <https://orcid.org/0000-0001-7036-2902>
 Bibhuti Kumar Jha  <https://orcid.org/0000-0003-3191-4625>
 Bidya Binay Karak  <https://orcid.org/0000-0002-8883-3562>
 Dipankar Banerjee  <https://orcid.org/0000-0003-4653-6823>

References

- Babcock, H. W. 1961, *ApJ*, 133, 572
 Caligari, P., Moreno-Insertis, F., & Schüssler, M. 1995, *ApJ*, 441, 886
 Cameron, R. H., & Schüssler, M. 2023, *SSRv*, 219, 60
 D’Silva, S., & Choudhuri, A. R. 1993, *A&A*, 272, 621
 Dasi-Espuig, M., Solanki, S. K., Krivova, N. A., Cameron, R., & Peñuela, T. 2010, *A&A*, 518, A7
 Fan, Y. 2009, *LRSP*, 6, 4
 Fan, Y., Fisher, G. H., & McClymont, A. N. 1994, *ApJ*, 436, 907
 Fisher, G. H., Fan, Y., & Howard, R. F. 1995, *ApJ*, 438, 463
 Hale, G. E., Ellerman, F., Nicholson, S. B., & Joy, A. H. 1919, *ApJ*, 49, 153
 Hoeksema, J. T., Liu, Y., Hayashi, K., et al. 2014, *SoPh*, 289, 3483
 Howard, R. F. 1991, *SoPh*, 136, 251
 Howard, R. F. 1996, *SoPh*, 169, 293
 Jha, B. K., Karak, B. B., Mandal, S., & Banerjee, D. 2020, *ApJL*, 889, L19
 Jha, B. K., Priyadarshi, A., Mandal, S., Chatterjee, S., & Banerjee, D. 2021, *SoPh*, 296, 25
 Karak, B. B. 2023, *LRSP*, 20, 3
 Karak, B. B., & Miesch, M. 2017, *ApJ*, 847, 69
 Karak, B. B., & Miesch, M. 2018, *ApJL*, 860, L26
 Kosovichev, A. G., & Stenflo, J. O. 2008, *ApJL*, 688, L115
 Leighton, R. B. 1964, *ApJ*, 140, 1547
 Longcope, D., & Choudhuri, A. R. 2002, *SoPh*, 205, 63
 Longcope, D. W., & Fisher, G. H. 1996, *ApJ*, 458, 380
 McClintock, B. H., & Norton, A. A. 2013, *SoPh*, 287, 215
 Parker, E. N. 1955, *ApJ*, 121, 491
 Scherrer, P. H., Bogart, R. S., Bush, R. I., et al. 1995, *SoPh*, 162, 129
 Scherrer, P. H., Schou, J., Bush, R. I., et al. 2012, *SoPh*, 275, 207
 Schunker, H., Baumgartner, C., Birch, A. C., et al. 2020, *A&A*, 640, A116
 Schunker, H., Birch, A. C., Cameron, R. H., et al. 2019, *A&A*, 625, A53
 Schüssler, M., & Rempel, M. 2005, *A&A*, 441, 337
 Sivaraman, K. R., Gokhale, M. H., Sivaraman, H., Gupta, S. S., & Howard, R. F. 2007, *ApJ*, 657, 592
 Sivaraman, K. R., Gupta, S. S., & Howard, R. F. 1999, *SoPh*, 189, 69
 Sreedevi, A., Jha, B. K., Karak, B. B., & Banerjee, D. 2023, *ApJS*, 268, 58
 Sreedevi, A. B., & Jha, B. K. 2023, *IAUS*, 372, 97
 Stenflo, J. O., & Kosovichev, A. G. 2012, *ApJ*, 745, 129
 Tian, L., Liu, Y., & Wang, H. 2003, *SoPh*, 215, 281
 Wang, Y. M., Colaninno, R. C., Baranyi, T., & Li, J. 2015, *ApJ*, 798, 50
 Wang, Y. M., & Sheeley, N. R. J. 1991, *ApJ*, 375, 761
 Weber, M. A., Fan, Y., & Miesch, M. S. 2011, *ApJ*, 741, 11
 Weber, M. A., Fan, Y., & Miesch, M. S. 2013, *SoPh*, 287, 239
 Will, L., Norton, A. A., & Hoeksema, J. T. 2023, arXiv:2310.20171
 Yeates, A. R. 2020, *SoPh*, 295, 119